

THE STRUCTURE OF BROWN DWARF CIRCUMSTELLAR DISKS

Christina Walker¹, Kenneth Wood¹, C.J. Lada², Thomas Robitaille¹, J.E. Bjorkman³, Barbara Whitney⁴

¹School of Physics & Astronomy, University of St. Andrews, North Haugh, St Andrews, KY16 9SS, Scotland;
cw26@st-andrews.ac.uk, kw25@st-andrews.ac.uk, tr9@st-andrews.ac.uk

²Harvard-Smithsonian Center for Astrophysics, 60 Garden Street, Cambridge, MA 02138; *clada@cfa.harvard.edu*

³Ritter Observatory, Department of Physics & Astronomy, University of Toledo, Toledo, OH 43606; *jon@astro.utoledo.edu*

⁴Space Science Institute, 3100 Marine Street, Suite A353, Boulder, CO 80303; *bwhitney@colorado.edu*

Released 2003 XXXXX XX

ABSTRACT

We present synthetic spectra for circumstellar disks that are heated by radiation from a central brown dwarf. Under the assumption of vertical hydrostatic equilibrium, our models yield scaleheights for brown dwarf disks in excess of three times those derived for classical T Tauri (CTTS) disks. If the near-IR excess emission observed from brown dwarfs is indeed due to circumstellar disks, then the large scaleheights we find could have a significant impact on the optical and near-IR detectability of such systems. Our radiation transfer calculations show that such highly flared disks around brown dwarfs will result in a large fraction of obscured sources due to extinction of direct starlight by the disk over a wide range of sightlines. The obscured fraction for a ‘typical’ CTTS is less than 20%. We show that the obscured fraction for brown dwarfs may be double that for CTTS, but this depends on stellar and disk mass. We also comment on possible confusion in identifying brown dwarfs via color-magnitude diagrams: edge-on CTTS display similar colors and magnitudes as a face-on brown dwarf plus disk systems.

Key words: circumstellar matter — infrared: stars — low mass, brown dwarfs — stars: pre-main-sequence

1 INTRODUCTION

Accumulating observational evidence indicates the presence of circumstellar disks around brown dwarfs, including near-IR (Oasa et al. 1999; Muench et al. 2001; Liu et al. 2003) and mid-IR excess emission (Comerón et al. 1998; 2000), and H α signatures of accretion (Muzerolle et al. 2000). The existence of circumstellar disks around brown dwarfs is an important discovery, since it may suggest that brown dwarfs form in a similar fashion to more massive T Tauri stars (Shu, Adams, & Lizano 1987). At the same time, data indicating significant masses and extents of circumstellar material may cause problems for brown dwarf formation scenarios where the low mass object is formed and subsequently ejected from multiple systems (Reipurth & Clarke 2001).

The observed spectral energy distributions (SEDs) and IR excess emission of some brown dwarfs have been modelled using flat and flared reprocessing disks (e.g., Natta & Testi 2001; Testi et al. 2002; Liu et al. 2003). The SED models suggest brown dwarf disks are similar to those around

CTTS. Models for the SEDs and scattered light images of CTTS require flared disks (e.g., Kenyon & Hartmann 1987; D’Alessio et al. 1999; Whitney & Hartmann 1992; Burrows et al. 1996). For highly inclined flared disks direct starlight is blocked by the optically thick disk resulting in a fraction of sources that will appear very faint in the optical and near-IR. Such faint or “optically obscured” sources may escape detection in magnitude limited surveys. The degree of disk flaring depends on the disk temperature structure and the mass of the central star, with the disk scaleheight $h \propto (T_d/M_*)^{1/2}$ (Shakura & Sunyaev 1973). Therefore, low mass brown dwarfs may have more vertically extended disks than those around CTTS and, depending on the disk mass, the obscured fractions may be larger. We will show that this may lead to confusion in discriminating between brown dwarfs and edge-on CTTS.

In this paper we adopt the same working hypothesis as Natta & Testi (2001) that brown dwarf disks are in vertical hydrostatic equilibrium with dust and gas well mixed throughout the disk. Such disk models have been very suc-

cessful in explaining the observed scattered light images and SEDs of CTTS. We extend our Monte Carlo radiative equilibrium code to calculate the structure of passively heated brown dwarf disks in vertical hydrostatic equilibrium. Our Monte Carlo radiation transfer technique naturally includes scattered light and the inclination dependence of the SED, which allows us to investigate the effects of highly flared disks. We construct synthetic spectral energy distributions and colors for disks of different sizes and masses surrounding brown dwarfs of different masses and luminosities. Our model SEDs enable us to determine to what extent observations in various spectral regions can diagnose disk parameters. Deriving disk parameters for large numbers of sources may help to discriminate brown dwarf formation mechanisms and whether they are different for dense and sparse star forming regions.

The layout of the paper is as follows: §2 outlines the ingredients of our models and the radiation transfer/disk density calculation, §3 presents disk structure models derived with our iterative technique, §4 presents our model SEDs and color-color diagrams, §5 compares our models with currently available observations of brown dwarf disks, and we summarize our results in §6.

2 MODEL INGREDIENTS

This study implements a number of extensions to the original Monte Carlo radiative equilibrium technique of Bjorkman & Wood (2001). These include a crude estimate of the inner disk radius (assumed to be at the dust destruction radius) and an improved temperature structure calculation. Our disks are not vertically isothermal or two-layered (Natta & Testi, 2001); 2D disk temperature structure is calculated in the MC simulation based on the technique described by Lucy (1999). Our code self-consistently determines the density structure of a passively heated disk in vertical hydrostatic equilibrium. The extensions to the radiation transfer technique are described in greater detail in the Appendix.

2.1 Disk Structure Calculation

Model SEDs are computed for a flared disk that is heated by radiation from a central brown dwarf. We only consider passive disks, since disk heating from viscous accretion is negligible compared to stellar heating in low accretion rate systems (Muzerolle et al. 2000; D’Alessio et al. 1999). Our disks extend from the dust destruction radius to an outer radius of 100AU. The disk is truncated sharply at its inner edge and there is no material between the inner edge and the star, equivalent to assuming material in this region is optically thin. In our previous modelling of CTTS SEDs (Wood et al. 2002a, b; Schneider et al. 2003; Grosso et al. 2003) we adopted the following flared disk density structure (e.g., Shakara & Sunyaev 1973)

$$\rho = \rho_0 \left(\frac{R_*}{\varpi} \right)^\alpha \exp - \frac{1}{2} [z/h(\varpi)]^2, \quad (1)$$

where ϖ is the radial coordinate in the disk midplane and the scaleheight increases with radius, $h = h_0 (\varpi/R_*)^\beta$. With the disk structure fixed we then calculate the temperature

structure and emergent SED using the Monte Carlo radiative equilibrium technique of Bjorkman & Wood (2001).

In this paper we adopt an iterative scheme to determine the disk density structure. Having calculated the disk temperature structure via our Monte Carlo radiative equilibrium technique, we impose vertical hydrostatic equilibrium and solve

$$\frac{dP}{dz} = -\rho g_z. \quad (2)$$

Here, $P = \rho c_s^2$ is the gas pressure, c_s is the isothermal sound speed, and $g_z = \frac{GM_* z}{\varpi^3}$ is the vertical component of gravity in the disk. We make the usual thin disk assumptions and assume the disk is non self-gravitating (Pringle 1981). We impose the boundary condition that the disk surface density $\Sigma \sim \varpi^{-1}$, in accordance with the detailed disk structure models of D’Alessio et al. (1999). Our simulations begin with the disk structure given by equation 1 with $\alpha = 2.25$, $\beta = 1.25$, and we iterate to derive a self-consistent vertical density structure. The density converges within three iterations.

In hydrostatic disk models, the disk scaleheight scales with radius as $h/\varpi = c_s/v_c$, where $c_s^2 = kT/\mu m_H$ and $v_c^2 = GM_*/\varpi$ are the isothermal sound speed and circular velocity at ϖ (e.g., Shakara & Sunyaev 1973; Lynden-Bell & Pringle 1974). For CTTS, $h(100\text{AU})$ is in the range 7AU to 20AU as found from radiative and hydrostatic equilibrium models (D’Alessio et al. 1999) and from fitting SEDs and scattered light images of disks using equation 1 with h_0 as a free parameter (Burrows et al. 1996; Stapelfeldt et al. 1998; Grosso et al. 2003; Schneider et al. 2003). However, for disks around brown dwarfs the scaleheights may be larger due to the smaller circular velocity of these low mass objects. If brown dwarf disks are indeed more vertically extended, then there may be a larger fraction of obscured brown dwarfs compared with CTTS. Our SED calculations enable us to address this issue.

2.2 Dust Parameters and Model Atmospheres

The circumstellar dust opacity and scattering properties are taken to be those of the dust size distribution we adopted for modelling the SEDs of HH 30 IRS and GM Aur (Wood et al. 2002a; Schneider et al. 2003; Rice et al. 2003). This dust model has a larger average grain size and a shallower wavelength dependent opacity than ISM dust models (e.g., Mathis, Rumpl, & Nordsieck 1977; Kim, Martin, & Hendry 1994). There is much observational evidence for large grains and a shallow wavelength dependent opacity in T Tauri disks (e.g., Beckwith et al. 1990; Beckwith & Sargent 1991; D’Alessio et al. 2000; Cotera et al. 2001; Wood et al. 2002a). The larger grain dust model we adopt does not exhibit strong silicate features (see Wood et al. 2002a).

The input stellar spectra for the brown dwarf models are the BD_Dusty model atmospheres presented by Allard et al. (2001), with $\log g = 3.5$ and effective temperatures of $T_* = 2200$ K, 2600 K and 2800 K. For CTTS models we use a 4000 K Kurucz model atmosphere (Kurucz 1994).

2.3 Parameter Space

We construct radiative and hydrostatic equilibrium models for brown dwarf systems with the range of stellar and circumstellar disk parameters given in Table 1. The stellar mass range of $0.01M_{\odot} \leq M_{\star} \leq 0.08M_{\odot}$ covers objects from the hydrogen burning limit down to the lower limit for brown dwarfs as identified via color-magnitude diagrams by Muench et al. (2001). The corresponding stellar radii and temperatures yield models representative of 1Myr old systems from the evolutionary tracks of Baraffe et al. (2002). For each set of stellar parameters, disk to star mass ratios of $\log(M_d/M_{\star}) = -1, -2$ and -3 are initially considered. The disk mass M_d refers to the total disk mass of dust and gas. As with our previous work, this mass does not include very large particles such as rocks or planetesimals and is therefore a lower limit. We compare our resulting brown dwarf disk structures with those of disks around a typical CTTS with $M_{\star} = 0.5M_{\odot}$, $R_{\star} = 2R_{\odot}$, and $T_{\star} = 4000$ K (e.g., Kenyon & Hartmann 1995; D'Alessio et al. 1999).

3 DISK STRUCTURE MODELS

At the end of our iterative procedure (described in the Appendix) the outputs of our code are the disk density and temperature structure and the emergent SED. All our brown dwarf models have Toomre parameter, $Q_{\star} > 1$, throughout their disks, so the thin disk assumption implicit in our models is still valid (e.g. D'Alessio et al. 1999). Fig. 1 shows scaleheights and mid-plane temperatures for disks of various masses illuminated by stars of different mass. The full disk structure is now calculated, however we choose to define scaleheight using the mid-plane temperature (see Appendix). For comparison we show the scaleheight and mid-plane temperature for a CTTS illuminating disks of the same mass ratio as in the brown dwarf models. The scaleheights of the CTTS disks are $h(100 \text{ AU}) \sim 15 \text{ AU}$, in agreement with the simulations of D'Alessio et al. (1999). The brown dwarf disks have scaleheights significantly in excess of those obtained for CTTS, with $h(100 \text{ AU})$ ranging from just over 20 AU for $M_{\star} = 0.08M_{\odot}$ to almost 60 AU for $M_{\star} = 0.01M_{\odot}$.

Our temperature calculations in Fig. 1 for brown dwarf disks show that $T(100 \text{ AU}) \sim 10 \text{ K}$ with little variation among the models. The stellar mass therefore predominantly controls the disk scaleheights. The brown dwarf models show disk scaleheights up to three times larger than for comparative disks illuminated by a CTTS. Such large scaleheights will result in a large range of viewing angles for which direct starlight will be extinguished by the disk. The effects of large scaleheights on the SED and colors are discussed in §4.

The extended nature of the brown dwarf disks is also clear in Fig 2 which shows K-band scattered light images of disks viewed at an inclination of 85° from face-on. As with CTTS models (Wood et al. 1998), the dust lane narrows with decreasing disk mass and the central source becomes increasingly more visible. Hence it seems that the detection of low mass disks via scattered light may only be possible for edge-on systems or if coronographic techniques are used to block the starlight.

4 MODEL SPECTRA AND COLORS

In addition to calculating the disk structure, our radiation transfer code outputs the SED for a range of viewing angles. This section shows SEDs and color-color diagrams that illustrate the main features of our models. With the Monte Carlo technique it is straightforward to determine the contributions to the SED of stellar, scattered, and thermally reprocessed photons (Wood et al. 2002a). We utilize this capability to determine the relative importance of the scattered light contribution to the SEDs and colors.

4.1 SEDs of Face-On Disks

Our brown dwarf model SEDs have similar spectral characteristics to those of CTTS disks (e.g., Wood et al. 2002b). Fig. 3 shows SEDs of face-on disks for a range of star and disk parameters. Face-on covers $0 \rightarrow 18^{\circ}$ due to binning of the photons in the Monte Carlo code. The dependence of SED on disk mass is readily evident and, as with CTTS, observations at long wavelengths provide the best diagnostics of disk mass.

As commented by Natta & Testi (2001) it is difficult to produce significant near-IR excesses for brown dwarfs because the stellar spectrum peaks at longer wavelengths than CTTS and can therefore dominate the disk thermal emission. At longer wavelengths however Fig. 3 shows that our brown dwarf models are capable of producing varying degrees of IR excess emission. As stellar mass decreases, scaleheights increase allowing the disk to intercept, scatter, and thermally reprocess more stellar radiation, which in turn gives rise to increasingly large IR excesses.

Fig. 4 shows the relative contribution of stellar, scattered, and thermal disk radiation for the highly flared $M_{\star} = 0.01M_{\odot}$, $T_{\star} = 2200$ K brown dwarf disk system with $\log(M_d/M_{\star}) = -1$ and includes a CTTS model for comparison. Scattered light makes little contribution to face-on models, but it can account for up to 90% of K-band flux as disks become more inclined (see Wood et al. 2002b, Fig. 9). The importance of including scattered light will be highlighted in §4.3.

Recent work on brown dwarf formation suggests that many brown dwarfs are ejected from multiple systems and that any circumstellar disks that survive the ejection will be very small. In the numerical simulations of Bate et al. (2003), no disks survive around ejected brown dwarfs down to their simulation resolution of ~ 10 AU. We have computed SEDs for disks of constant mass, but varying R_d in the range 10AU - 200AU. Because M_d was held constant in these models, smaller R_d yields larger optical depths. The SEDs are mostly unaltered as R_d changes apart from some variation at far-IR/sub-mm wavelengths. We conclude that it would be very difficult to determine disk radii from SED data alone and more stringent tests of the small disks prediction of Bate et al. (2003) will require high resolution imaging to resolve the disks via their scattered light and thermal emission (see also, Beckwith et al. 1990; Chiang et al. 2001).

4.2 Near-IR Color-Color Diagrams

By far the most popular technique of identifying circumstellar disks is to identify sources with near-IR excess emission

in color-color diagrams (e.g., Lada & Adams 1992; Rebull et al 2002). It was through near-IR color-magnitude and color-color diagrams that Meunck et al. (2001) and Liu et al. (2003) identified many candidate brown dwarfs that exhibit the tell-tale IR excess emission indicative of circumstellar disks.

All colors we present are relative to Vega and are computed using 2MASS JHK and UKIRT L filter transparency curves. The BD_Dusty model atmospheres that we use have near-IR colors that are bluer than observations of the corresponding spectral type (e.g., Bessell & Brett 1988; Kirkpatrick et al. 2000). What is important is the relative color of our models (e.g., $[H - K] - [H - K]_*$) and the underlying stellar spectrum does not affect this. As we ultimately compare our models with observations, we have used a similar approach to Liu et al. (2003) and applied a color offset to the models so that the model stellar colors match observations. We adopt spectral types of M9.5, M8.5 and M6 for our 2200, 2400 and 2800 K models respectively. There is no well defined temperature scale for M dwarfs and so classifications were chosen on consideration of observations and discussion by Luhman (1999), Pavlenko et al (2000) and Dahn et al (2002). We shift the stellar colors of our models to match the field M dwarf locus taken from Bessell & Brett (1988) and average colors from Kirkpatrick et al. (2000). This results in the following offsets for the M9.5, M8.5 and M6 fits: $\Delta(J - H) = 0.34, 0.23, 0.10$, $\Delta(H - K) = 0.12, 0.06, 0.00$. No shift in K-L is applied.

Fig. 5 shows JHK and $JHKL$ color-color diagrams for our model disks viewed face-on, and following the afore mentioned adjustments. In general, excess emission is more readily detected at long wavelengths (e.g. Haisch, Lada, & Lada 2000, Natta & Testi 2001) and this is again seen here with models showing larger excesses at $K - L$ than at $J - H$ or $H - K$. The trend of our models is that the more massive and more flared disks exhibit the largest IR excesses. Inclination effects yield a spread in color-color diagrams and we explore this in the next section.

4.3 Inclination, Scattered Light, and Obscured Fractions

For highly inclined CTTS, direct starlight is blocked by the optically thick disk and such systems will be very faint in the optical and near-IR (e.g., D'Alessio et al. 1999; Wood et al. 2002a, b). Compared to CTTS, the larger disk scaleheights we derive for the brown dwarf models will result in a larger fraction of viewing angles over which the central starlight is blocked by the disk. For the purpose of this study we define an “obscured source” to be one where the near-IR flux is at least three magnitudes fainter than the corresponding face-on source. The obscured fraction therefore depends on the disk size, mass, and scaleheight. For CTTS, the obscured fraction is around 20% (D'Alessio et al. 1999; Wood et al. 2002b) for disks of $M_d \sim 10^{-3} M_\odot$.

Figure 6 shows the inclination effect on the SEDs for various brown dwarf disk models. The SEDs are shown for ten viewing angles evenly spaced in $\cos i$, so that each curve represents 10% of sources by number if we assume sources are randomly distributed in inclination angle. We find obscured fractions from 20% to 60% with highly inclined sources only detected in the near-IR via scattered

light and weak thermal emission. The largest obscured fraction occurs for the lowest stellar mass of $M_* = 0.01 M_\odot$ with $\log(M_d/M_*) = -1$ and $T_* = 2200$ K. The smallest obscured fraction occurs for the highest stellar mass of $M_* = 0.08 M_\odot$ with $\log(M_d/M_*) = -3$ and $T_* = 2800$ K.

Studies of the initial mass function in Trapezium, ρ Ophiucus and IC348 show a relatively flat distribution over the range $0.08 \leq M_*(M_\odot) \leq 0.04$ and then a sharp fall off below this (Luhman 2000; Muench et al. 2002). If the IMF is flat and the fall-off due to small number statistics then within a young cluster population up to 55% of brown dwarf candidates, as defined by our parameter range, may be obscured. This is an upper limit produced using maximum obscuration fractions for each stellar mass assuming a disk to stellar mass ratio of $\log(M_d/M_*) = -1$. For a declining IMF, and a distribution of disk masses, the obscured fraction will be less. Within our parameter range a minimum of 20% of sources are likely to be obscured regardless of stellar mass distribution and assuming disk to stellar mass ratios of $\log(M_d/M_*) = -3$.

The relatively low luminosity of brown dwarfs and the increased obscuration due to highly flared disks may present detection problems. At a distance of 150pc (as used in Fig. 6) it would be possible to detect some obscured sources in the K band assuming a sensitivity limit of 16.5 mags. In the absence of high resolution imaging however these sources may be incorrectly identified as low luminosity systems. A three fold increase in distance would be sufficient to make all obscured sources undetectable at this sensitivity limit.

Figure 7 shows the inclination dependence in the brown dwarf $JHKL$ color-color diagrams. Relative colors are plotted for ten inclinations with the change in color at each inclination indicated by an arrow. Similar to the behaviour observed by Kenyon et al. (1993) and Whitney et al. (1997) we see a loop in the color-color plane with inclination. Starting from face-on, the sources generally get redder with increasing inclination and then loop around and end up with edge-on sources being slightly bluer than face-on, but still redder than the intrinsic stellar colors. Edge-on sources are seen almost entirely via scattered light. Note that these are slightly redder than the star because the scattered light, which is relatively blue, suffers extinction and becomes somewhat reddened. This trend is seen in all of the models.

Figure 8 contains data for the same model as in Fig. 7, but also shows the change in color with inclination if scattered light is ignored. The removal of scattered light makes the colors much redder, with the effect being particularly significant at moderate to high inclinations. This emphasizes the importance of including scattering when creating and studying models of such systems.

4.4 CTTS/Brown Dwarf Confusion

When only unresolved photometry is available our models show that edge-on CTTS could be mistaken as brown dwarfs. CTTS have edge-on flux levels that are comparable to face-on brown dwarfs and similar colors. Muench et al. (2001) identified sources within the Trapezium cluster with $13.5 \lesssim H \lesssim 17.5$ as candidate brown dwarfs. They note that 21 of their 109 brown dwarf candidates are coincident with optically resolved proplyds (Bally, O'Dell, & McCaughean 2000; O'Dell & Wong 1996) and 21% of the candidates that

exhibit IR excess, indicative of circumstellar disks, are represented by these proplyds. In the absence of high resolution imaging the task of identifying faint sources such as brown dwarfs may be problematic. If no central star is seen then these sources could be edge-on CTTS that happen to have the same magnitude and colors as a pole-on brown dwarf and disk. This confusion could lead to an overestimation of brown dwarf numbers.

5 COMPARISON TO OBSERVATIONS

This section compares our synthetic models and published observations of suspected brown dwarf disks. For the Chameleon cluster the SED data is taken from Comerón et al (2000) and Apai et al (2002); ρ Ophiucus data comes from Barsony et al. (1997), Comerón et al (1998), Bontemps et al (2001) and Natta et al (2002). JHKL data is taken from the above papers along with Kirkpatrick et al (2000) and Liu et al.(2003). All near-IR photometry has been converted to the 2MASS system (Carpenter, 2001).

5.1 Spectral Energy Distributions

Figure 9 shows flared disk model fits to the SED data for candidate brown dwarfs in the ρ Ophiucus and Chameleon star clusters. Table 2. contains details of the model parameters used to produce the fits. We used stellar parameters from Natta & Testi (2001) and Natta et al (2002) as starting points for each of our models.

Natta & Testi (2001) modelled Cha H α 1, 2, & 9 using a flared disk model. Their models produced a successful fit in the MIR region of the spectrum and predicted a strong $10\mu\text{m}$ silicate emission feature. Apai et al (2002) later made observations of Cha H α 2 at 9.8 and $11.9\mu\text{m}$ and did not detect the silicate feature. They presented an optically thick flat disk model which produced no silicate feature. The SEDs of ρ Oph sources have been modelled by Natta et al. (2002) and they found indications that as many as eight of these stars may have flat disks.

Our models open up the possibility that the absence of a silicate feature may be explained with larger circumstellar dust grains. In addition, low mass disks may fit SEDs previously modelled with flat disks. As Fig. 9 demonstrates, it is possible to fit the observed data for all sources with a flared disk geometry. The use of larger grains naturally suppresses the silicate feature which has been shown to be missing from the Chameleon data and low mass disks of $10^{-5}M_{\odot}$ and $10^{-7}M_{\odot}$ allow us to fit the IR data of the candidates where flat disks were previously suspected. We note that many of these fits have disk to stellar mass ratios outside the typical range of $-1 \leq \log(M_d/M_{\star}) \leq -3$ (Natta et al. 2000; Klein et al. 2003) and flat disks (Natta et al. 2002) remain a possibility.

Another alternative, testable with long wavelength observations, is that steeper surface density profiles can also be used to fit the data with higher mass disks. In Fig. 10, ISO#030 has been modelled using both surface density $\Sigma \sim \varpi^{-1}$ and $\Sigma \sim \varpi^{-2}$. Using $\Sigma \sim \varpi^{-2}$ allows us to fit the data with a disk eight times more massive disk than used in the $\Sigma \sim \varpi^{-1}$ case. Both models fit the data well in the NIR/MIR, but are quite different in the FIR. Long

wavelength observations would help to discriminate between flat disk, low mass flared disks and steeper surface density disk models.

If lower mass flared models are representative of disks in brown dwarf populations, as opposed to higher mass disks, then problems with obscuration may not be as significant as suggested in §4.3. Equally flat disks do not result in severe obscuration of the central star unless at very high inclinations.

Figure 11 shows the derived scaleheights for the disks that we used to model the observed SEDs of Fig. 9 and Fig. 10. This illustrates the range of disk structures that can produce fits to the observed data. In each plot the scaleheight of a model CTTS of corresponding disk to stellar mass ratio is presented as a comparison. For these models we find scaleheights up to three times that of the corresponding CTTS.

5.2 JHKL colors

Figure 12 shows JHKL plots of our face-on models and published data. Following the adjustments discussed in §4.2, Fig. 11 shows that our models (if reddening were included) can reproduce the observed spread in colors of suspected brown dwarf disk systems. Including all inclinations (Fig. 13) allows for the redder colors of inclined disks and produces a spread in the JHKL plots that is in very good agreement with the observed colors.

Figure 13 also shows the CTTS locus taken from Meyer et al. (1997). This again demonstrates that there is an overlap between CTTS and brown dwarf colors which may lead to incorrect identification of sources if only color-magnitude data is available.

6 SUMMARY

We have presented model SEDs and color-color diagrams for brown dwarf disks. The main assumptions in our models are that the disks are in vertical hydrostatic equilibrium with dust and gas well mixed throughout. Our models are self-consistent and employ an iterative procedure to determine the hydrostatic density structure for passively heated disks. Compared to CTTS, brown dwarf disks have larger scaleheights due to the lower mass of the central star. In some cases the scaleheights of brown dwarf disks are more than three times larger than for the same disk to stellar mass ratio for a CTTS. The larger scaleheights result in more inclinations over which the direct stellar radiation is blocked or obscured by the flared disk. The fraction of optically obscured systems depends on the stellar mass and disk optical depth and in our models is in the range $20\% \leq f_{\text{obs}} \leq 60\%$. For a typical CTTS about 20% of sources will be optically obscured.

If, as our models suggest, brown dwarf disks are highly flared, detection of brown dwarf disk systems will be biased towards face-on systems. We also show that without direct imaging or spectroscopic identification, it will be difficult to distinguish between edge-on CTTS and face-on brown dwarfs. Color-color diagrams show that edge-on sources, which are only detected in the optical/near-IR via scattered light, have similar colors to face-on sources. This may lead

to incorrect identification of sources. In particular, we find that an edge-on CTTS will have similar near-IR magnitudes and colors as face-on brown dwarf disk systems.

We compare our synthetic models to SED and color-color observations of suspected brown dwarfs and show that flared disks of varying mass can account for the observed SEDs and colors. Our adopted circumstellar dust model naturally suppresses the $10\mu\text{m}$ silicate feature that is absent in the observations of Cha H α 2. Long wavelength observations are required to discriminate between our flared disk models and alternative flat disk models that have been proposed for some sources.

We acknowledge financial support from a UK PPARC Studentship (CW); UK PPARC Advanced Fellowship (KW); NASA's Long Term Space Astrophysics Research Program, NAG5 8412 (BW), NAG5 8794 (JEB); the National Science Foundation, AST 9909966 (BW), AST 9819928 (JEB).

REFERENCES

- Allard, F., Hauschildt, P.H., Alexander, D.R., Tamanai, A., & Schweitzer, A., 2001, ApJ, 556, 357
- Apai, D., Pascucci, I., Henning, Th., Sterzik, M.F., Klein, R., Semenov, D., Gunther, E., & Sterzik, B., 2002, ApJ, 573L, 115
- Bally, J., O'Dell, C.R., & McCaughrean, M.J., 2000, AJ, 119, 2919
- Baraffe, I., Chabrier, G., Allard, F., & Hauschildt, P.H., 2002, A&A, 382, 563
- Barsony, M., Kenyon, S.J., Lada, E.A., & Teuban, P.J., 1997, ApJs, 112, 109
- Bate, M.R., Bonnell, I.A., & Bromm, V., 2003, MNRAS, 339, 577
- Beckwith, Steven V.W., Sargent, A.I., Chini, R.S., & Guesten, R., 1990, AJ, 99, 924
- Beckwith, S.V.W., & Sargent, A.I., 1991, ApJ, 381, 205
- Bessell, M.S., & Brett, J.M., 1988, PASP, 100, 1134
- Bjorkman, J.E., & Wood, K., 2001, ApJ, 554, 615
- Bontemps, S., André, P., & Kaas, A.A., et al., 2001, A&A, 372, 173
- Burrows, C.J., et al., 1996, ApJ, 473, 437
- Cardelli, J.A., Clayton, G.C., & Mathis, J.S., 1989, 345, 245
- Carpenter, John M., 2001, AJ, 121, 2851
- Chiang, E.I., Joung, M.K., Creech-Eakman, M.J., Qi, C., Kessler, J.E., Blake, G.A., & van Dishoeck, E.F., 2001, ApJ, 547, 1077
- Comerón, F., Rieke, G.H., Claeis, P., Torra, J., & Laureijs, R.J., 1998, A&A, 335, 522
- Comerón, F., Neuhauser, R., & Kaas, A.A., 2000, A&A, 359, 269
- Cotera, A.S., et al., 2001, ApJ, 556, 958
- Dahn, C. C., et al., 2002, AJ, 124, 1170
- D'Alessio, P., Cantó, J., Hartmann, L., Calvet, N., & Lizano, S., 1999, ApJ, 511, 896
- D'Alessio, P., Calvet, N., & Hartmann, L., 2000, AAS, 196, 408
- Grosso, N., Alves, J., Wood, K., Neuhauser, R., Montmerle, T., & Bjorkman, J.E., 2003, ApJ, 586, 296
- Haisch, K.E., Jr., Lada, E.A., & Lada, C.J. 2000, AJ, 120, 1396
- Kenyon, S.J., & Hartmann, L., 1987, ApJ, 323, 714
- Kenyon, S.J., & Hartmann, L., 1995, ApJS, 101, 117
- Kenyon, S.J., Whitney, B.A., Gómez, M., & Hartmann, L., 1993, ApJ, 414, 773
- Kim, S.-H., Martin, P.G., & Hendry, P.D., 1994
- Kirkpatrick, J.D., Reid, I.N., Liebert, J., Gizis, J.E., Burgress, A.J., Monet, D.G., Dahn, C.C., Nelson, B., & Williams, R.J., 2000, AJ, 120, 447
- Klein, R., Apai, D., Pascucci, I., Henning, Th., & Waters, L.B.F.M., 2003, ApJ, 593, L57
- Kurucz, R. L. 1994, CD-ROM 19, Solar Abundance Model Atmospheres (Cambridge: SAO)
- Lada, C. J., & Adams, F. C. 1992, ApJ, 393, 278
- Liu, M.C., Najita, J., & Tokunaga, A.T., 2003, ApJ, 585, 372
- Lucy, L.B., 1999, A&A, 344, 282
- Luhman, K.L., 1999, ApJ, 544, 1044
- Luhman, K.L., 2000, ApJ, 544, 1044
- Luhman, K.L., Briceño, C., Rieke, G.H., & Hartmann, L., 1998a, ApJ, 493, 909
- Lynden-Bell, D., & Pringle, J.E., 1974, MNRAS, 168, 603
- Martín, E.L., Dougados, C., Magnier, E., Ménard, F., Magazzù, A., Cuillandre, J.-C., & Delfosse, X. 2001, ApJ, 561, L195
- Mathis, J.S., Rumpl, W., & Nordsieck, K.H., 1977, 217, 425
- Meyer, M.R., Calvet, N., & Hillenbrand, L.A., 1997, AJ, 114, 288
- Muench, A.A., Alves, J., Lada, C.J., & Lada, E.A., 2001, ApJ, 558, 51
- Muench, A.A., Lada, E.A., Lada, C.J., & Alves, J., 2002, ApJ, 573, 366 (Paper I)
- Muzerolle, J., Briceño, C., Calvet, N., Hartmann, L., Hillenbrand, L., & Gullbring, E., 2000, ApJ, 545, L141
- Najita, J.R., Tiede, G.P., & Carr, J.S., 2000, ApJ, 541, 977
- Natta, A., Grinin, V.P., & Mannings, V., 2000, in Protostars and Planets IV, ed. V. Mannings, A. Boss, & S.S. Russell (Tucson: Univ. Arizona Press), 559
- Natta, A., & Testi, L., 2001, A&A, 376, L22
- Natta, A., Testi, L., Comerón, F., Oliva, E., D'Antona, F., Baffa, C., Comoretto, G., & Gennari, S., 2002, A&A, 393, 597
- Oasa, Y., Tamura, M., & Sugitani, K., 1999, ApJ, 526, 336
- O'Dell, C.R., & Wong, K. 1996, AJ, 111, 846
- Pavlenko, Y., Zapatero Osorio, M.R., & Rebolo, R., 2000, A&A, 355, 245
- Pringle, J.E., 1981, ARA&A, 19, 137
- Rebull, L.M., et al., 2002, AJ, 123, 1528
- Reipurth, B., & Clarke, C., 2001, AJ, 122, 432
- Rice, W.K.M., Wood, K., Armitage, P.J., Whitney, B.A., Bjorkman, J.E., 2003, MNRAS, 342, 79
- Schneider, G., Wood, K., Silverstone, M.D., Hines, D.C., Koerner, D.W., Whitney, B.A., Bjorkman, J.E., & Lowrance, P.J., 2003, AJ, 125, 1467
- Shakura, N.I., & Sunyaev, R.A., 1973, A&A, 24, 337
- Shu, F.H., Adams, F.C., & Lizano, S., 1987, ARA&A, 25, 23
- Stapelfeldt, K.R., Krist, J.E., Menard, F., Bouvier, J., Padgett, D.L., & Burrows, C.J., 1998, ApJ, 502, L65
- Testi, L., Natta, A., Oliva, E., D'Antona, F., Comerón, F.,

- Baffa, C., Comoretto, G., Gennari, S., 2002, ApJ, 571L, 155
 Whitney, B.A., & Hartmann, L., 1992, ApJ, 395, 529
 Whitney, B.A., Kenyon, S.J., & Gomez, M., 1997, ApJ, 485, 703
 Wood, K., Kenyon, S.J., Whitney, B., & Turnbull, M., 1998, ApJ, 497, 404
 Wood, K., Wolff, M.J., Bjorkman, J.E., & Whitney, B.A., 2002a, ApJ, 564, 887
 Wood, K., Lada, C.J., Bjorkman, J.E., Kenyon, S.J., Whitney, B., & Wolff, M.J., 2002b, ApJ, 567, 1183

APPENDIX

MONTE CARLO RADIATION TRANSFER CODE DEVELOPMENTS

A1. DENSITY STRUCTURE

In this study we determine the structure of circumstellar disks based on the assumption that the disk is in vertical hydrostatic equilibrium with dust and gas well mixed. We therefore solve the hydrostatic equilibrium equation

$$\frac{dP}{dz} = -\rho g_z , \quad (\text{A-1})$$

where P is the pressure, ρ is the density, and g_z is the vertical component of gravity in the disk. Conservation of mass in the disk is enforced by keeping the radial dependence of the surface density.

The hydrostatic equation has an analytic solution if the disk temperature is assumed to be vertically isothermal at any given cylindrical radius, ϖ . Using the mid-plane temperature, $T(\varpi)$, the disk density has a Gaussian distribution about the midplane with scaleheight

$$h(\varpi) = \left(\frac{k T(\varpi) \varpi^3}{G M_\star \mu m_H} \right)^{\frac{1}{2}} , \quad (\text{A-2})$$

where k and G are the Boltzmann and Newton constants, m_H is the mass of hydrogen and μ is the molecular weight of disk material and is taken to be $\mu = 2.3$ for a molecular hydrogen/helium combination.

In order to solve for the density numerically, we approximate the integral of equation A-1 to a sum of finite contributions. Using the equation of state, $P = \rho c_s^2$, where $c_s^2 = kT/\mu m_h$ is the local sound speed squared, this leads to

$$\ln \left(\frac{\rho}{\rho_0} \right) = - \sum \frac{1}{T} \left(\frac{dT}{dz} + \frac{g_z \mu m_H}{k} \right) \Delta z \quad (\text{A-3})$$

which can be solved using

$$\frac{dT}{dz} = \cos \theta \frac{dT}{dr} - \frac{\sin \theta}{r} \frac{dT}{d\theta} \quad (\text{A-4})$$

In the discretization of the disk density we use a spherical polar grid (Whitney & Wolf 2002) throughout which we calculate g_z at the midpoint of each cell. The cell temperature determined from our radiative equilibrium calculation is assumed to be uniform within each cell and Δz is the incremental distance through each cell which lies directly below grid centre (r, θ, ϕ) . It is therefore possible to obtain values of ρ/ρ_0 for each grid cell.

We assume the disk surface density has the form, $\Sigma(r) = \Sigma_0(\varpi/R)^{-1}$, which agrees with the disk structure models of D'Alessio et al. (1999). Since total disk mass is given by

$$M_d = \int_{R_{min}}^{R_{max}} \Sigma(\varpi) 2\pi \varpi d\varpi , \quad (\text{A-5})$$

we can solve for Σ_0 and in turn get $\Sigma(\varpi)$. We then normalize ρ_0 so that surface density is a constant,

$$\rho_0(\varpi) = \frac{\Sigma_0 (R/\varpi)}{\sum \rho/\rho_0 \Delta z} \quad (\text{A-6})$$

For each cell ρ/ρ_0 and the cylindrical radius, ϖ , are known, so we may therefore determine the density in each cell.

A2. TEMPERATURE STRUCTURE

In order to determine the density structure we require an accurate calculation of the disk temperature structure. While the Bjorkman & Wood (2001) technique yields accurate SEDs, we found that the temperature calculation was too noisy for use in our density calculation. Increasing the number of photon energy packets yields a smoother temperature structure at the cost of a large increase in CPU time. We have therefore implemented the temperature calculation technique of Lucy (1999), which is based on using an estimator for the mean intensity of the radiation field. Integrating this technique into our Monte Carlo code leads to a higher signal-to-noise in the disk temperature determination with fewer photon packets. What follows is an outline of the procedure we use and we refer the reader to Lucy (1999) for more details.

Provided a system is in radiative equilibrium, the rate at which matter absorbs energy from the radiation field is balanced by the rate at which matter emits energy, $\dot{A} = \dot{E}$ or,

$$4\pi \int_0^\infty \rho(1 - a_\nu) \kappa_\nu J_\nu d\nu = 4\pi \int_0^\infty \rho(1 - a_\nu) \kappa_\nu B_\nu d\nu \quad (\text{A-7})$$

As discussed by Lucy (1999) the mean intensity, J_ν and therefore heating is proportional to the photon path lengths, l , through the cells yielding,

$$\dot{A} = \frac{\epsilon}{\delta t \delta V} \sum l \rho(1 - a_\nu) \kappa_\nu , \quad (\text{A-8})$$

where δt is the cell simulation time, δV is the cell volume, a_ν is the scattering albedo, and κ_ν is the total opacity in cm^2/g . The energy of each photon packet is $\epsilon = L \delta t / N$, where L is the source luminosity and N is the number of Monte Carlo photon packets used in our simulation. The expression for the rate at which matter emits energy can also be simplified to:

$$\dot{E} = 4\pi \rho \kappa_P B(T) \quad (\text{A-9})$$

where κ_P is the Planck mean absorption coefficient and $B(T) = \sigma T^4 / \pi$ is the integrated Planck function. Equating A-7 and A-8 leads to the following expression for temperature:

$$T^4 = \left(\frac{\dot{A}}{4\kappa_p(T)\sigma} \right) . \quad (\text{A-10})$$

Since $\kappa_P(T)$ is a function of temperature we solve this equation iteratively using pre-tabulated values of $\kappa_P(T)$.

Our code uses the Bjorkman & Wood (2001) technique for reprocessing photon packets and our modification of Lucy's (1999) pathlength technique to determine the cell temperature. Since we assume the opacity is not a function of temperature, we do not need to iterate to determine the temperature structure, as discussed in Bjorkman & Wood (2001).

A3. DUST DESTRUCTION

Model disks used in this study extend from a sharply cut-off inner radius out to a specified distance. The inner radius is defined by the dust destruction temperature which we take to be 1600 K. We make the simplifying assumption that the dust destruction radius is independent of latitude in the disk. The determination of the dust destruction radius is carried out after the temperature calculation and involves a nested loop that counts how many grid cells at each radius have temperatures below 1600K. If this number is outside some specified range then the inner radius is shifted either towards or away from the central star. The disk density is then regridded and the temperature calculation/dust destruction radius determination repeated. This continues until a stable radius is established. Once the inner radius is fixed the program starts to iteratively solve for density as described above.

A4. ITERATIVE PROCEDURE

The program self-consistently solves for density using an iterative procedure. For the first iteration the analytic density structure of Eq. 1 is assumed and this allows an initial temperature structure to be found. On the next iteration or at the point at which a suitable dust destruction radius has been established and a new grid set-up, this temperature structure is used to determine a density structure using the numerical density technique. This density replaces the analytic density structure and the next iteration begins. The procedure continues until the temperature and density structure converges, typically within three iterations.

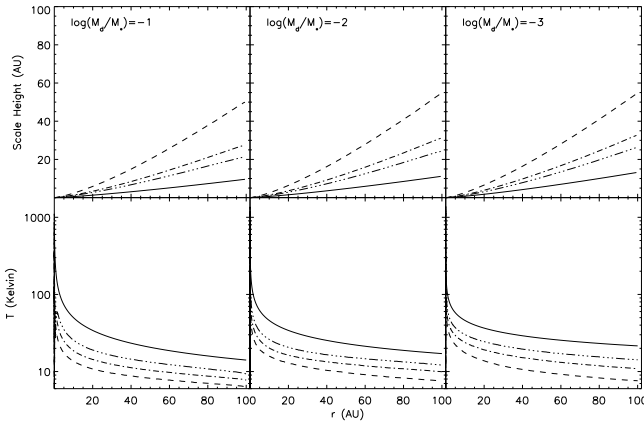


Figure 1. Upper: Scaleheights of brown dwarf models compared to CTTS models with matching disk mass. Lower: Mid-plane temperatures. In each plot the dashed, dot-dashed and triple dot dashed lines represent central stars of mass $0.01M_{\odot}$, $0.04M_{\odot}$ and $0.08M_{\odot}$ respectively and the solid line represents the CTTS model. The disk to stellar mass ratio is indicated in each panel.

Table 1. Model Parameters

M_{\star} (M_{\odot})	T_{\star} (K)	R_{\star} (R_{\odot})	L_{\star} (L_{\odot})
0.01	2200	0.25	0.0013
0.04	2600	0.50	0.0038
0.08	2800	0.90	0.044

Table 2. Model Fit Parameters

Object	T_{\star} (K)	R_{\star} (R_{\odot})	M_{\star} (M_{\odot})	M_d (M_{\odot})	A_v (mags)	Inclination (deg)
ISO#023	2600	0.95	0.04	10^{-5}	8	0
ISO#030	2600	1.2	0.08	10^{-5}	2	0
ISO#032	2600	1.2	0.08	10^{-5}	3	0
ISO#033	2200	0.63	0.01	10^{-3}	7	0
ISO#102	3000	1.17	0.08	10^{-7}	3.5	0
ISO#160	2600	0.95	0.08	10^{-7}	6	0
ISO#164	2600	1.36	0.08	10^{-3}	4	63
ISO#176	3000	1.17	0.08	10^{-7}	7	60
ISO#193	3000	1.5	0.08	10^{-5}	7	78
CHA H α 1	2600	0.5	0.01	10^{-5}	0.3	0
CHA H α 2	2600	1.05	0.04	10^{-5}	1.1	37
CHA H α 9	2600	0.95	0.08	10^{-5}	3.2	72

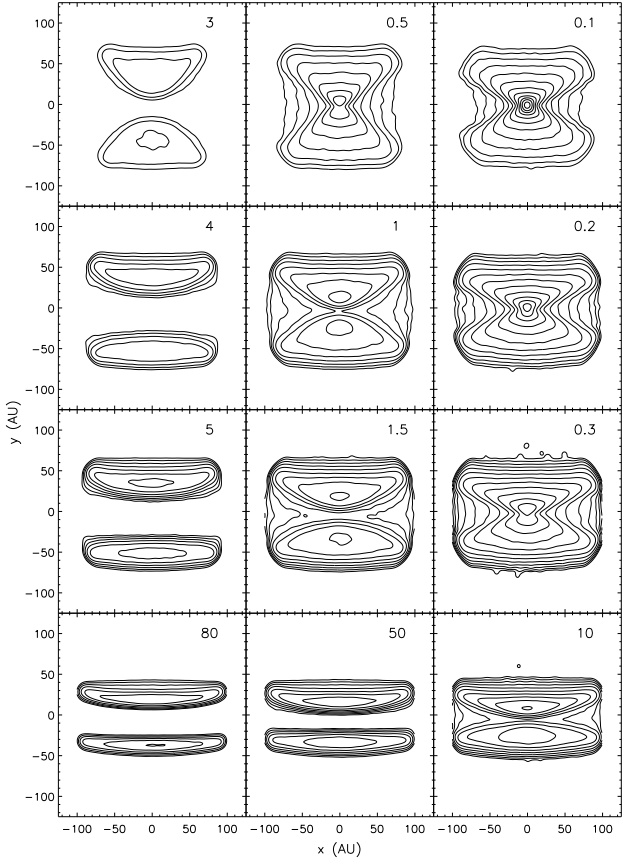


Figure 2. K-band contour plots of 9 brown dwarf models and 3 comparison CTTS models. In declining order each row represents models of stellar mass 0.01 , 0.04 , and $0.08 M_{\odot}$ and the bottom row is the CTTS model. Moving from left to right each column represents models with $\log(M_d/M_{\star})=-1$, -2 , and -3 . The number in each panel is the lowest contour level in $\mu\text{Jy}/\text{arcsec}^2$, assuming source is at 150pc. Contours increase in 1 mag intervals.

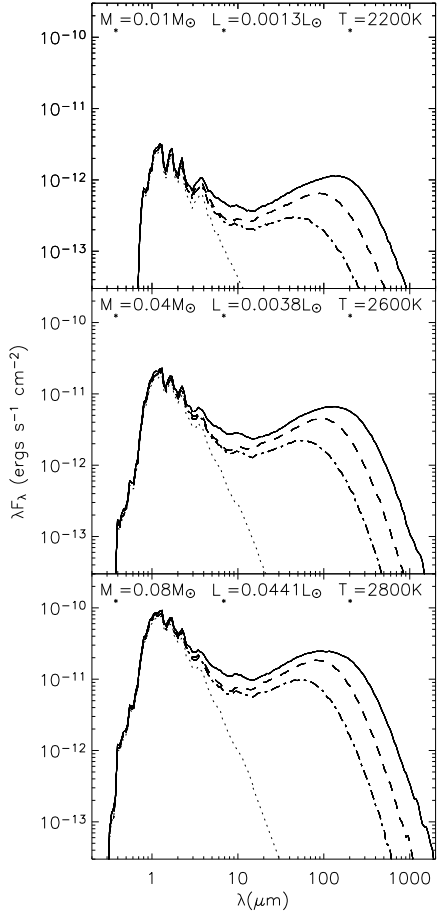


Figure 3. Face-on model SEDs showing the effects of varying stellar properties and disk mass. Each plot contains three separate SEDs for $\log(M_d/M_\star) = -1$ (solid line), -2 (dashed line) and -3 (dot-dash line). The dotted line represents the input stellar spectrum. Other parameters are as described in the text.

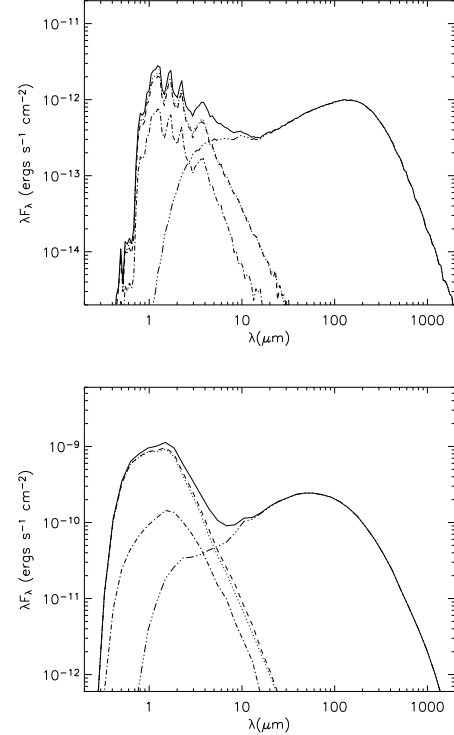


Figure 4. SEDs showing contributions from direct (dashed line), scattered (dot-dashed line) and disk reprocessed photons (triple dot-dash line) along with the input stellar spectrum (dotted line) and the total SED (solid line). Upper: brown dwarf model with $M_\star = 0.01M_\odot$, $\log(M_d/M_\star) = -1$ and $L_\star = 0.0013L_\odot$. Lower: CTTS model with $\log(M_d/M_\star) = -1$

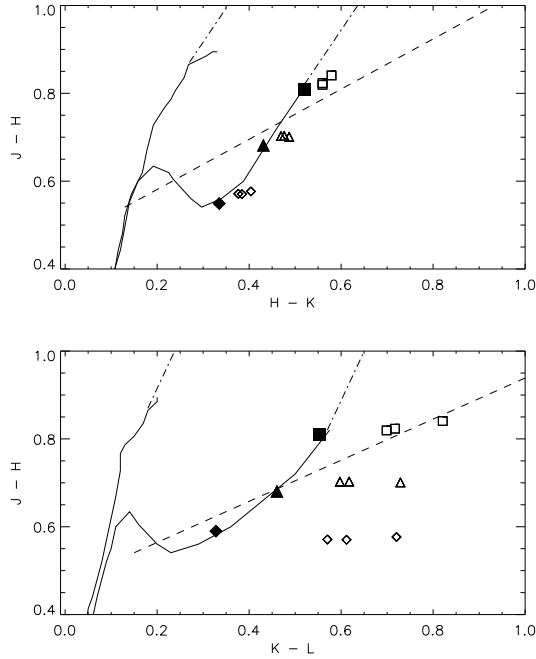


Figure 5. JHKL color-color diagrams containing face-on colors for brown dwarf models with different T_* , M_d and M_* . The reddest colors correspond to low stellar masses and therefore highly flared disks. The filled symbols of corresponding shape represent the average stellar color of all models at fixed temperatures of 2200 K, 2600 K and 2800 K. The CTTS locus (dashed line) is taken from Meyer et al. (1997). The giant branch and M dwarf locus (solid lines) are taken from Bessell & Brett (1988) and Kirkpatrick et al. (2000). The dot-dash lines represent reddening vectors. Models have been shifted so that average stellar colors lie on the “brown dwarf locus”.

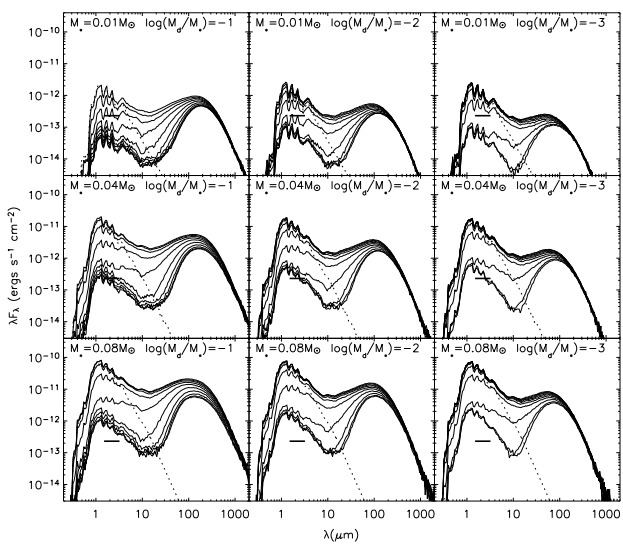


Figure 6. SEDs illustrating obscured fractions for our grid of brown dwarf models. Obscured fractions range from 20% up to 60% whereas comparable CTTS models show 20%. The greatest obscuration in a brown dwarf model occurs for the lowest stellar mass of $M_* = 0.01M_\odot$, with $\log(M_d/M_*) = -1$ and $T_* = 2200$ K/ L_* = 0.0013 L_\odot . Least obscuration occurs for the highest stellar mass of $M_* = 0.08M_\odot$, with $\log(M_d/M_*) = -3$ and $T_* = 2800$ K/ L_* = 0.044 L_\odot . The thick horizontal solid line represents a detection limit of 16.5 mags at K.

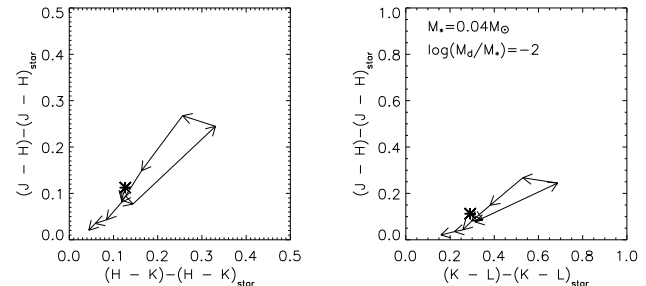


Figure 7. JHKL plot for the $M_* = 0.04M_\odot$ and $\log(M_d/M_*) = -2$ brown dwarf model. Arrows indicate the change in colors as inclination varies from nearly edge-on (indicated by bold asterisk) to face-on and colors are relative to central star’s colors. This plot is indicative of the behaviour of all the brown dwarf models.

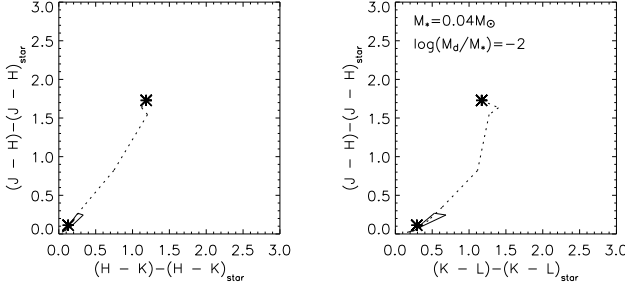


Figure 8. JHKL plots as in Fig. 7, but also with dotted lines showing the change at each inclination that would result if scattering effects were removed.

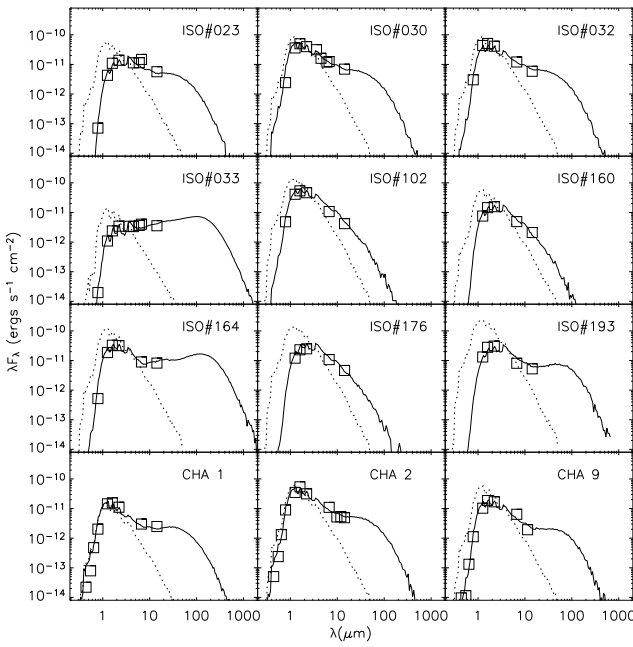


Figure 9. Models SED fits to observed data in ρ Ophiucus and Chameleon star clusters as indicated. All models are of a flared disk around a central star with an inner gap of radius $2R_*$. A distance of 150pc is assumed for both clusters. Further model parameters are given in Table. 2. The dotted line represents the input spectrum. For ISO#030 two models are presented. In all cases a solid line indicates surface density $\Sigma \sim \varpi^{-1}$. For ISO#030 the dashed line indicates $\Sigma \sim \varpi^{-2}$. The data is not corrected for the effects of reddening, instead the models are reddened according to Cardelli, Clayton and Mathis (1989) with $R_v = 4$.

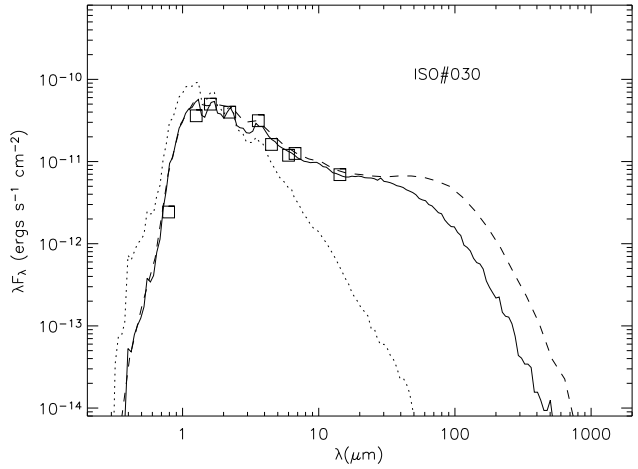


Figure 10. Models SED fits as in Fig. 9. Two models are presented for ISO#030. The solid line indicates surface density $\Sigma \sim \varpi^{-1}$. The dashed line indicates $\Sigma \sim \varpi^{-2}$. Model parameters for $\Sigma \sim \varpi^{-1}$ case are given in Table. 2. The $\Sigma \sim \varpi^{-2}$ model has a disk eight time more massive.

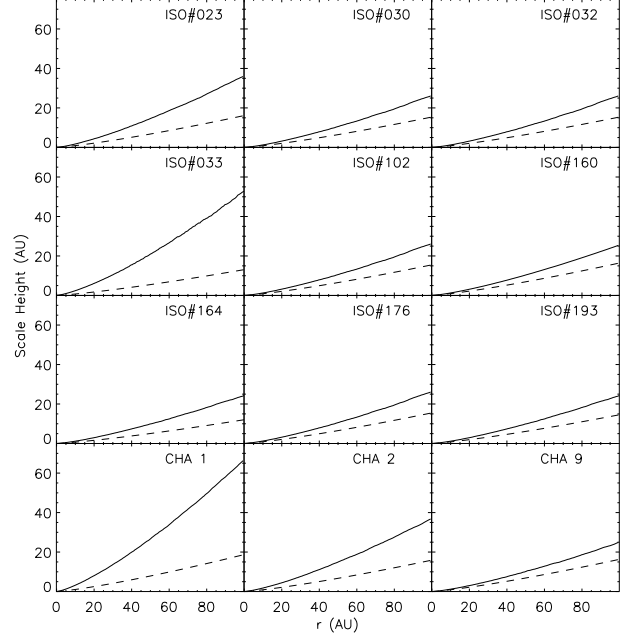


Figure 11. Scaleheights for our models (solid lines) presented in Fig. 9. The scaleheight for our 'typical CTTS' at matching disk to stellar mass ratio is given as a comparison (dashed line). For ISO#030 scaleheights are virtually coincident for the two models presented in Fig. 10 and therefore only the $\Sigma \sim \varpi^{-1}$ case is shown here.

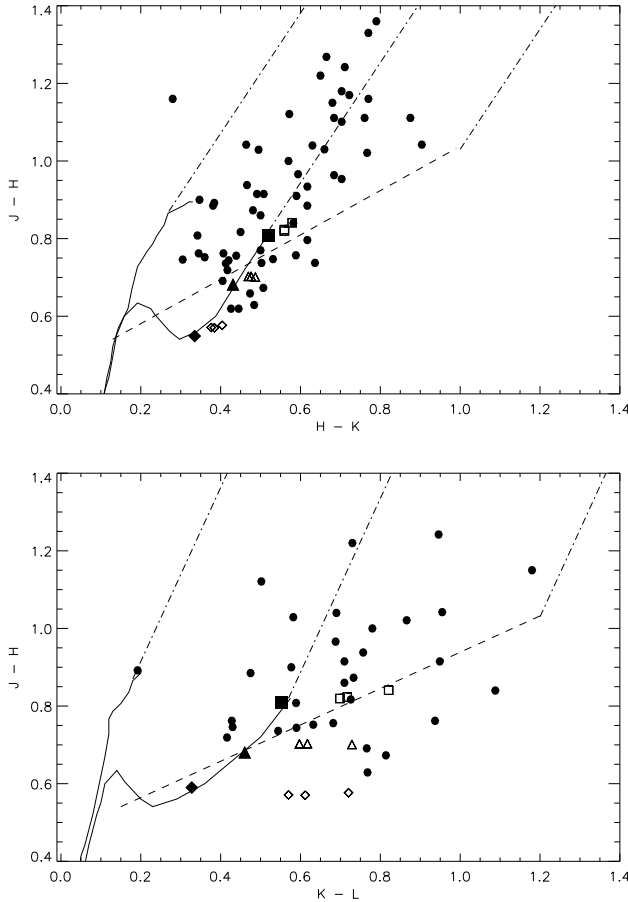


Figure 12. JHKL plots containing observed (\bullet) and face-on model (square, triangle, diamond) colors. Where possible data was obtained directly from the 2MASS second incremental data release (Carpenter, 2001). Remaining data was retrieved from the papers of Comerón et al (1998/2000), Martín et al (2000), Briceño et al (1998), Luhman et al (1998a), Luhman (1999), Najita et al (2000) and Liu et al (2003). As previously the solid shapes represent the average stellar color obtained for models of $T_\star = 2200$, 2600 and 2800 K. The CTTS locus (dashed line) is taken from Meyer et al. (1997). The giant branch and M dwarf locus (solid lines) are taken from Bessell & Brett (1988) and Kirkpatrick et al. (2000). The dot-dash lines represent reddening vectors. Models have been shifted so that stellar colors lie on the “brown dwarf locus”.

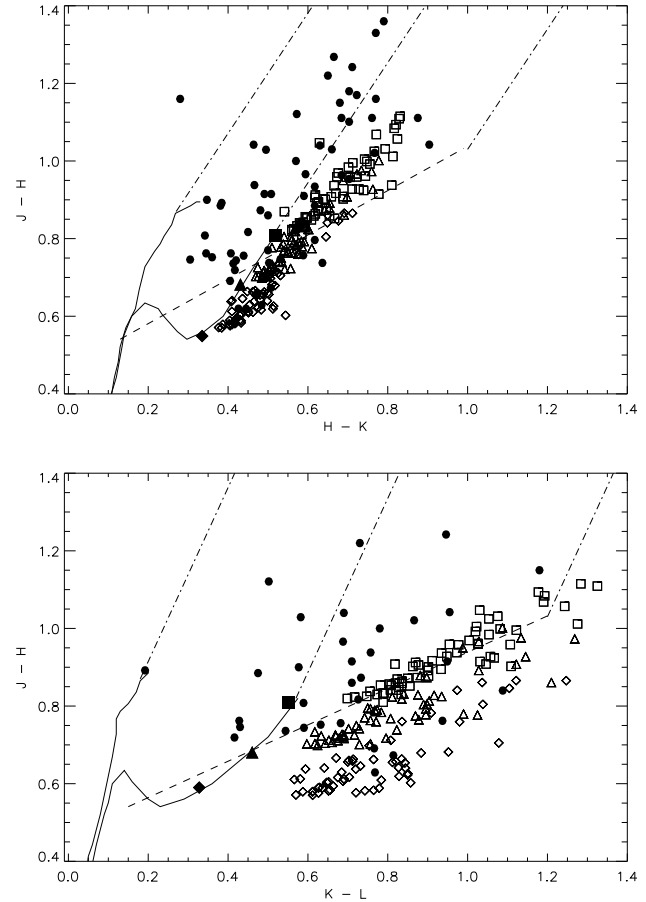


Figure 13. JHKL plots as in Fig. 12, but with model colors for all inclinations.